

Article

Effect of Cr and Mo Substitution of Fe on Activation and Hydrogen Ab-/Desorption Properties of TiFe Hydrogen Storage Alloy

Yuehai Li ¹, Houqun Xiao ², Minglong Zhong ^{1,*} and Qingjun Chen ^{3,*}

¹ Jiangxi Province Key Laboratory of Magnetic Metallic Materials and Devices, School of Materials Science and Engineering, Jiangxi University of Science and Technology, Ganzhou 341000, China

² School of Intelligent Manufacturing and Materials Engineering, Gannan University of Science and Technology, Ganzhou 341000, China

³ Key Laboratory of Rare Earths, Jiangxi Institute of Rare Earths, Ganjiang Innovation Academy, Chinese Academy of Sciences, Ganzhou 341000, China

* Correspondence: memlzhong@126.com (M.Z.); qjchen@gia.cas.cn (Q.C.)

Abstract: In this study, a series of quaternary TiFe-based alloys, $Ti_{1.05}Fe_{0.85}Cr_{0.1-x}Mo_x$ ($x = 0, 0.03, 0.05, 0.07, 0.1$), were designed to investigate the activation and hydrogen ab-/desorption properties of TiFe hydrogen storage alloys through the substitution of Fe with Cr and Mo. The incorporation of Cr and Mo significantly enhanced the activation performance of TiFe hydrogen storage alloys, enabling activation at room temperature. This improvement in activation was accompanied by the maintenance of a high maximum hydrogen storage capacity and an elevated effective hydrogen storage capacity. As the Mo content increased, the lattice parameters increased slightly, further boosting the activation performance and reducing the optimal operating temperature from 90 to 75 °C, which can be readily matched using the waste heat from fuel cells. The addition of Mo also resulted in a flatter hydrogen absorption plateau, making the hydrogen storage and release process more stable. Among the alloys, $Ti_{1.05}Fe_{0.85}Cr_{0.05}Mo_{0.05}$ exhibited the best performance, with a maximum hydrogen storage capacity of 2.00 wt.%, an effective hydrogen storage capacity of 1.81 wt.%, and a relatively flat hydrogen ab-/desorption plateau. After 200 cycles, the hydrogen storage capacity decreased by only 0.50%, indicating promising application prospects in related fields.



Received: 26 January 2025

Revised: 10 February 2025

Accepted: 12 February 2025

Published: 14 February 2025

Citation: Li, Y.; Xiao, H.; Zhong, M.; Chen, Q. Effect of Cr and Mo Substitution of Fe on Activation and Hydrogen Ab-/Desorption Properties of TiFe Hydrogen Storage Alloy. *Metals* **2025**, *15*, 200. <https://doi.org/10.3390/met15020200>

Copyright: © 2025 by the authors. Licensee MDPI, Basel, Switzerland. This article is an open access article distributed under the terms and conditions of the Creative Commons Attribution (CC BY) license (<https://creativecommons.org/licenses/by/4.0/>).

1. Introduction

With the continuous growth of the global population, energy demand is forced to grow sharply. Renewable and clean energy, which is environmentally friendly, widely distributed, and suitable for local exploitation and utilization [1], mainly includes solar energy [2,3], wind energy [4], ocean energy [5], and others sources. However, the collection and utilization of these energy sources have certain limitations, such as dependence on time (day and night, seasons), weather, and geographical factors [6]. Hydrogen energy, as a secondary energy source, can be effectively coupled with the aforementioned renewable energies. These renewable energies can be converted into hydrogen, which can then be utilized more efficiently at appropriate times or in specific scenarios [7–10].

The storage methods of hydrogen energy generally include gaseous hydrogen storage (compressed hydrogen), liquid hydrogen storage (liquefied hydrogen), solid-state hydrogen

storage (metal hydrides), organic liquid hydrogen storage, and others. Among these, solid-state hydrogen storage stands out due to its advantages such as high volumetric hydrogen storage density, high energy efficiency, good safety, and lower costs. It is considered one of the most promising hydrogen storage methods and is highly suitable for the conversion and storage of hydrogen and renewable energy in fixed scenarios [11]. Solid-state hydrogen storage materials typically include Mg-based hydrogen storage alloys (Mg_2Ni , MgH_2 , etc.) [12–14], BCC (V-based) hydrogen storage alloys [14], Ti-based hydrogen storage alloys ($TiFe$, $TiMn_2$, etc.) [15,16], and rare-earth hydrogen storage alloys like $LaNi_5$ [17].

$TiFe$ -type hydrogen storage alloys exhibit a simple cubic $CsCl$ -type structure with a theoretical hydrogen storage capacity of 1.9 wt.%. After activation, they demonstrate favorable kinetic and thermodynamic properties, enabling hydrogen absorption and desorption reactions at room temperature [18]. However, challenges such as difficult activation and susceptibility to impurity gas poisoning have hindered their widespread application [19]. To address these shortcomings, scientists have conducted numerous studies to improve the activation performance and poison resistance of $TiFe$ -type hydrogen storage alloys. Techniques such as element doping or substitution, ball milling, and rapid solidification have been widely employed [20]. For instance, the use of transition metal elements such as Cr, Mn, Co, and Ni has significantly enhanced both activation performance and poison resistance. Activation performance has been improved from requiring multiple hydrogen absorption and desorption cycles at 773 K before modification to completion of activation within three cycles at 573 K, albeit with a reduction in the maximum hydrogen storage capacity [17,21–25]. Further improvements have been achieved by incorporating rare-earth elements such as Ce, La, and Y. These additions allow for direct hydrogen absorbing at room temperature, although it is often accompanied by a longer incubation period and a decrease in the maximum hydrogen storage capacity [25–29]. Non-stoichiometric Ti contributions to $TiFe$ alloys have also been explored, demonstrating improvements in activation performance and increased maximum hydrogen storage capacity. Nevertheless, drawbacks remain, such as a slanted hydrogen absorption plateau and a larger residual hydrogen storage amount [30–33]. It has been observed that while improving activation performance, hydrogen storage and desorption properties are typically compromised. A perfect solution that benefits both aspects has yet to be discovered.

Therefore, this study aims to identify a method to maximize the activation performance of $TiFe$ -type hydrogen storage alloys while minimizing or eliminating declines in their hydrogen storage and desorption properties. By considering the impact of Cr on the activation performance of $TiFe$ and the influence of excess Ti, various strategies, including the co-substitution of Fe with both Cr and Mo elements and incorporating excess Ti, were employed. Consequently, a series of quaternary alloys with the composition $Ti_{1.05}Fe_{0.85}Cr_{0.1-x}Mo_x$ ($x = 0, 0.03, 0.05, 0.07, 0.1$) were designed. For ease of subsequent discussion, these alloys are abbreviated as $Cr_{0.1}$, $Cr_{0.07}Mo_{0.03}$, $Cr_{0.05}Mo_{0.05}$, $Cr_{0.03}Mo_{0.07}$, and $Mo_{0.1}$, respectively.

2. Experimental Section

2.1. Preparation of $Ti_{1.05}Fe_{0.85}Cr_{0.1-x}Mo_x$ Hydrogen Storage Alloys

A series of alloys with the composition $Ti_{1.05}Fe_{0.85}Cr_{0.1-x}Mo_x$ ($x = 0, 0.03, 0.05, 0.07, 0.1$) were designed by maintaining a Ti excess and co-substituting Fe with both Cr and Mo elements. All five alloy samples were prepared using a low-voltage arc melting furnace under an argon atmosphere, employing raw materials of Ti (99.9%), Fe (99.9%), Cr (99.95%), and Mo (99.9%). Each button was presented with dimensions of $h = 1.2$ cm and $d = 1.9$ cm and was weighed at approximately 15 g. Prior to melting, a 15 g Zr ingot was melted to remove oxygen from the furnace chamber. After obtaining the final alloy ingots, they

underwent heat treatment at 1273 K for 24 h and were subsequently allowed to cool naturally to room temperature. The heat-treated alloy ingots were then encapsulated in vacuum bags and stored in a glovebox.

2.2. Material Characterization

The compositional analysis of the samples was conducted utilizing an X-ray fluorescence spectrometer (XRF; ZSXPrimusIII+, Rigaku Corporation from Tokyo, Japan). The phase structures were determined by an X-ray diffractometer (XRD; Empyrean, PANalytical, Malvern Panalytical from Almelo, The Netherlands) using Cu K α radiation at 40 kV and 20 mA, with a scan range of $2\theta = 15\text{--}90^\circ$, a scan speed of 0.02° per second, and a step size of 0.04° . The morphologies of the samples were observed by scanning electron microscopy (SEM, JSM-IT800, JEOL Ltd. from Tokyo, Japan). High-resolution electron microscopy (HRTEM) was performed with the JEOL-2100F instrument (JEOL Ltd. from Tokyo, Japan). Meanwhile, selected area electron diffraction (SAED) patterns were characterized to confirm local compositional information and phase microstructure. The elemental compositions of each phase constituting the alloy were then evaluated using energy-dispersive spectroscopy (EDS) manufactured by Oxford Instruments (Oxford Instruments plc, from Oxford, UK) and an electronic probe microanalyzer (EPMA; JXA-iSP100; JEOL Ltd. from Tokyo, Japan).

2.3. Performance Test

Before performance testing, the ingots were removed from the glovebox, and the surface oxide layer was removed. The ingots were then crushed and sieved through an 80-mesh screen. Between 1.5 and 2 g of powder was taken and subjected to isothermal kinetic and PCT (Pressure-Composition-Temperature) tests using the MH-PCT equipment (General Research Institute for Nonferrous Metals Research Group Co., Ltd from Beijing, China). The PCT tests were conducted at four temperatures: 298 K, 323 K, 348 K, and 363 K. For cycling performance evaluation, the semi-automatic cycling mode of the MH-PCT was utilized. After full hydrogen absorption, the pressure in the reactor was maintained at 3 MPa. Desorption was performed at 573 K for 9 min, followed by hydrogen absorption at room temperature for 21 min, with each cycle lasting half an hour and a maximum of 200 cycles conducted. PCT curves were measured before and after cycling to compare the decay in maximum hydrogen storage capacity.

3. Results and Discussion

3.1. Microscopic Structure and Phase Composition

The composition of the $\text{Ti}_{1.05}\text{Fe}_{0.85}\text{Cr}_{0.1-x}\text{Mo}_x$ ($x = 0, 0.03, 0.05, 0.07, 0.1$) alloys was analyzed by an XRF (X-ray fluorescence spectrometer), and the results are presented in Table 1. The actual compositions of all elements were close to the designed compositions.

Table 1. The actual compositions of all alloys analyzed by XRF.

Samples	Ti	Fe	Cr	Mo
$\text{Cr}_{0.1}$	1.052	0.849	0.099	0.000
$\text{Cr}_{0.07}\text{Mo}_{0.03}$	1.046	0.847	0.077	0.030
$\text{Cr}_{0.05}\text{Mo}_{0.05}$	1.049	0.844	0.050	0.056
$\text{Cr}_{0.03}\text{Mo}_{0.07}$	1.051	0.843	0.031	0.074
$\text{Mo}_{0.1}$	1.049	0.845	0.000	0.105

The crystal structure of the alloys was analyzed using an X-ray diffractometer (XRD) in a previous study. Figure 1 showcases the XRD diffraction patterns within an angular range

of $15\text{--}90^\circ$, where Figure 1a displays the distinctive diffraction peaks of TiFe at $42.6 \pm 0.04^\circ$ (110), $61.92 \pm 0.04^\circ$ (200), and $78.12 \pm 0.04^\circ$ (211). Furthermore, a minor diffraction peak at $40.12 \pm 0.04^\circ$ (110), corresponding to both the $\text{Ti}_{0.8}\text{Fe}_{0.2}$ phase and the β -Ti phase, was observed. The positions of the diffraction peaks associated with the β -Ti phase and the $\text{Ti}_{0.8}\text{Fe}_{0.2}$ phase indicated that their strongest peaks were situated very close to each other, jointly contributing to the intensity of this smaller diffraction peak. Figure 1b,c depict the XRD diffraction patterns of $\text{Cr}_{0.1}$, $\text{Cr}_{0.05}\text{Mo}_{0.05}$, and $\text{Mo}_{0.1}$, respectively, after refinement was conducted using GSAS-II (revision:5765) software. The refined phase compositions and lattice parameters are tabulated in Table S1, while the refined XRD diffraction patterns of $\text{Cr}_{0.07}\text{Mo}_{0.03}$ and $\text{Cr}_{0.03}\text{Mo}_{0.07}$ are presented in Figure S1.

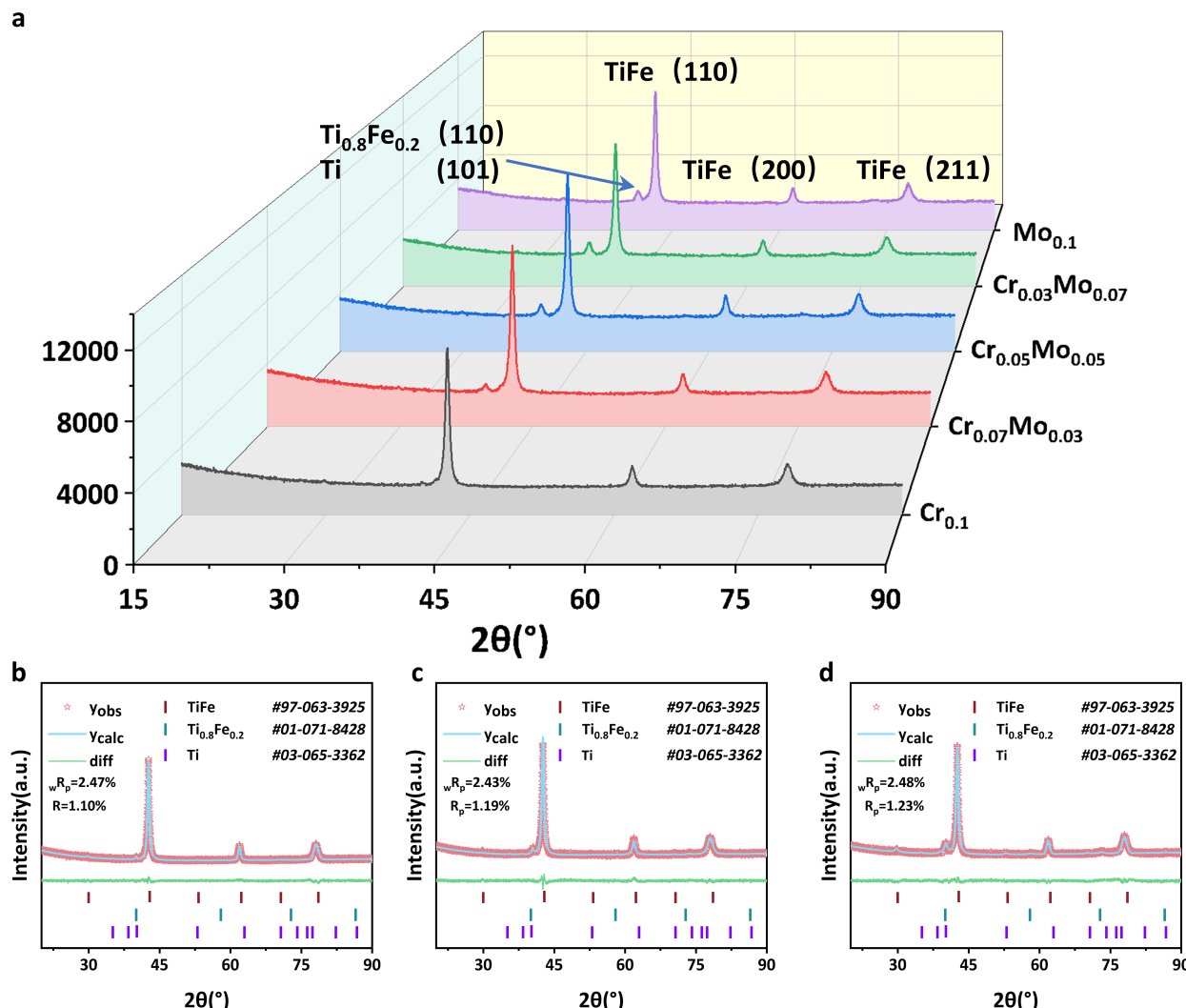


Figure 1. (a) Comparison of XRD patterns of different components of the alloys; the result of GSAS-II finishing was (b) $\text{Cr}_{0.1}$, (c) $\text{Cr}_{0.05}\text{Mo}_{0.05}$, and (d) $\text{Mo}_{0.1}$.

Each sample exhibited three phases: the TiFe phase, the $\text{Ti}_{0.8}\text{Fe}_{0.2}$ phase, and the β -Ti phase, with phase abundances fluctuating within ranges of 80–81%, 9–11%, and 9–11%, respectively. The lattice parameter of pure TiFe is 0.2976 nm, that of the pure $\text{Ti}_{0.8}\text{Fe}_{0.2}$ phase is 0.3180 nm, and that of the β -Ti phase is 0.2950 nm, respectively. Compared to the lattice parameters of the pure phases, all samples exhibit an increase in the lattice parameter of the TiFe main phase and a decrease in that of the $\text{Ti}_{0.8}\text{Fe}_{0.2}$ phase and β -Ti phase. This is due to the substitution of Fe with Cr or Mo, with the atomic radius of Cr and Mo being larger than that of Fe but smaller than that of Ti, resulting in an increase in the lattice parameters of

the TiFe main phase. The substitution of Ti by Cr and Mo leads to a decrease in the lattice parameters of the $\text{Ti}_{0.8}\text{Fe}_{0.2}$ phase, which are all smaller than those of the pure phase, which can be explained by the results of XRD combined with SEM-EDS point scanning (Table 2) of the dark gray areas. The decrease in lattice parameters of the β -Ti phase is attributed to the substitution of Ti in the β -Ti phase by Cr, Mo, and Fe. With the introduction of Mo, and due to the larger atomic radius of Mo compared to Cr, the lattice parameters of various phases increase as the substitution amount of Mo increases. The phase distribution and crystal structures of the alloys were characterized using SEM and TEM. Figure 2a–e show SEM-BSE images, each containing three distinct contrast phases. The largest area occupied by the light gray phase corresponds to the primary TiFe phase, followed by the darker gray $\text{Ti}_{0.8}\text{Fe}_{0.2}$ phase. The smallest area, which is black, represents the β -Ti phase. This observation is consistent with the results obtained from the refined XRD data. A summary of the EDS point scan data is presented in Table 3, with elemental compositions similar to the refinement results. Interestingly, Cr and Mo are used to substitute Fe in the TiFe main phase, whereas in the $\text{Ti}_{0.8}\text{Fe}_{0.2}$ phase, they substitute Ti instead. With the addition of Mo, cracks formed around the $\text{Ti}_{0.8}\text{Fe}_{0.2}$ phase in the $\text{Cr}_{0.05}\text{Mo}_{0.05}$ alloy, which were absent in the $\text{Cr}_{0.1}$ and $\text{Mo}_{0.1}$ alloys. These cracks can provide more pathways for hydrogen to enter the alloy's interior.

Table 2. Element composition of each region after SEM-EDS point scanning.

Samples	Area	Elements (± 0.01 at %)			
		Ti	Cr	Fe	Mo
$\text{Cr}_{0.1}$	Black	90.57	1.47	7.95	/
	Dark grey	73.00	5.71	21.29	/
	Light gray	51.67	5.04	43.29	/
$\text{Cr}_{0.07}\text{Mo}_{0.03}$	Black	93.90	0.69	5.06	0.35
	Dark grey	76.43	3.82	17.78	1.97
	Light gray	52.30	3.87	42.33	1.50
$\text{Cr}_{0.05}\text{Mo}_{0.05}$	Black	89.77	0.67	9.02	0.54
	Dark grey	76.62	2.66	19.28	1.44
	Light gray	52.01	2.48	42.92	2.59
$\text{Cr}_{0.03}\text{Mo}_{0.07}$	Black	86.88	0.99	8.87	3.26
	Dark grey	77.12	1.31	19.79	1.78
	Light gray	52.28	1.77	42.30	3.64
$\text{Mo}_{0.1}$	Black	86.00	/	12.70	1.30
	Dark grey	76.00	/	21.70	2.30
	Light gray	52.09	/	43.33	4.58

Table 3. Summary of maximum and effective hydrogen storage capacity of different components at different temperatures.

Sample	298 K		323 K		348 K		363 K	
	(a) Max. wt.%	(b) Eff. wt.%	Max. wt.%	Eff. wt.%	Max. wt.%	Eff. wt.%	Max. wt.%	Eff. wt.%
$\text{Cr}_{0.1}$	1.97	0.68	2.02	0.84	2.05	1.55	1.93	1.74
$\text{Cr}_{0.07}\text{Mo}_{0.03}$	1.93	0.66	1.94	1.03	1.85	1.67	1.69	1.49
$\text{Cr}_{0.05}\text{Mo}_{0.05}$	1.99	0.71	2.00	0.98	1.92	1.74	1.69	1.56
$\text{Cr}_{0.03}\text{Mo}_{0.07}$	1.90	0.62	1.92	1.61	1.72	1.50	1.63	1.46
$\text{Mo}_{0.1}$	1.91	0.69	1.88	1.58	1.60	1.36	1.50	1.28

(a) Maximum hydrogen storage capacity. (b) Effective hydrogen storage capacity.

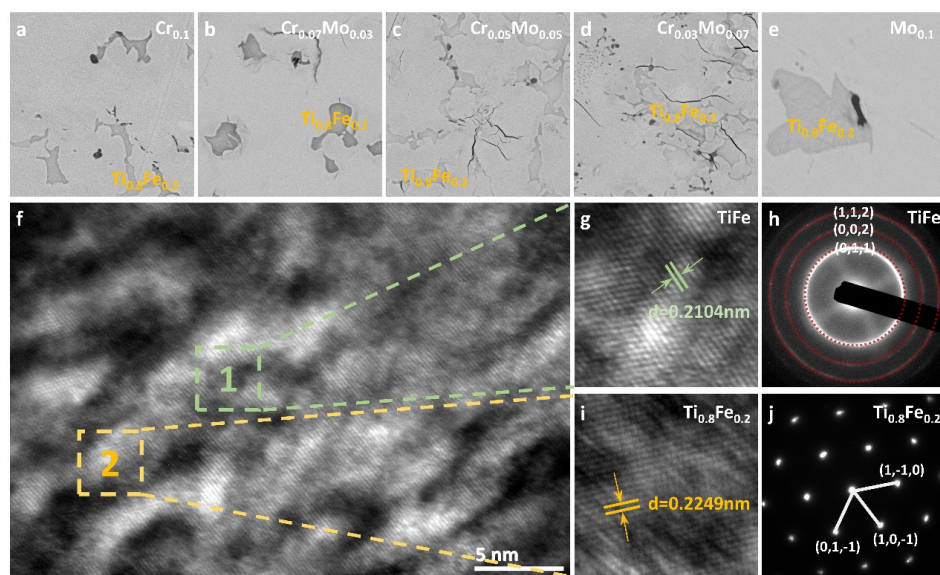


Figure 2. SEM-BSE images (**a–e**) are Cr_{0.1}, Cr_{0.07}Mo_{0.03}, Cr_{0.05}Mo_{0.05}, Cr_{0.03}Mo_{0.07}, and Mo_{0.1}, respectively. (**f**) HRTEM bright-field phase; (**g,i**) local detail enlarged image; (**h,j**) HRTEM diffraction rings and diffraction spots.

Figure 2f–j display the HRTEM bright-field and dark-field images of the Cr_{0.05}Mo_{0.05} alloy. The analysis using DigitalMicrograph (DMS-3) software revealed a lattice spacing of $d = 0.2104$ nm in Figure 2g, with the diffraction rings in Figure 2h identified as the TiFe phase. Figure 2i,j show a lattice spacing of $d = 0.2249$ nm for the Ti_{0.8}Fe_{0.2} phase. Figure S2a–f present HRTEM images of the Cr_{0.1} and Mo_{0.1} alloys, exhibiting the same structures as observed in the Cr_{0.05}Mo_{0.05} alloy.

To further analyze the role of Mo in the alloys, the EPMA was used to scan the elemental distribution in the Cr_{0.1}, Cr_{0.05}Mo_{0.05}, and Mo_{0.1} alloys. Figure 3 shows the elemental mapping images. Specifically, Figure 3b,g,l and Figure 3c,h,m depict the distribution of Ti and Fe elements, respectively. The composition of the red regions in Ti and the blue regions in Fe roughly aligns with the results obtained from SEM point scanning. Comparative analysis of Figure 3d,i,j,o reveals that the element Cr is distributed around the Ti_{0.8}Fe_{0.2} phase within the alloy, while Mo is primarily located within the Ti_{0.8}Fe_{0.2} phase. The element Mo mainly substitutes Fe in the Ti_{0.8}Fe_{0.2} phase, further increasing lattice distortion and leading to crack formation. This also indirectly confirms that Mo substitutes Ti within the Ti_{0.8}Fe_{0.2} phase.

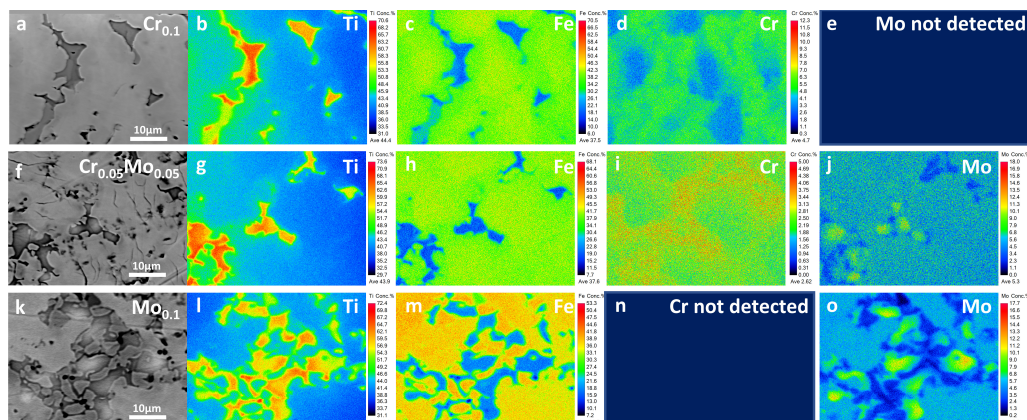


Figure 3. EPMA surface scan images of different components: BSE Images (**a,f,k**) and Elemental Mapping images of Ti (**b,g,l**), Fe (**c,h,m**), Cr (**d,i,n**), and Mo (**e,j,o**) for Compositions of Cr_{0.1}, Cr_{0.05}Mo_{0.05}, and Mo_{0.1}.

3.2. Ab-/Desorption Activation, Kinetics, and Thermodynamics Performance

Figure 4f displays the initial hydrogen absorption kinetics curves of the alloys at 298 K. It can be observed that all alloys can directly absorb hydrogen at room temperature. The induction period for hydrogen absorption in Cr_{0.1} is 15 min. With the addition of Mo, the activation performance gradually improves, due to the continuous increase in lattice parameters, leading to enhanced activation properties.

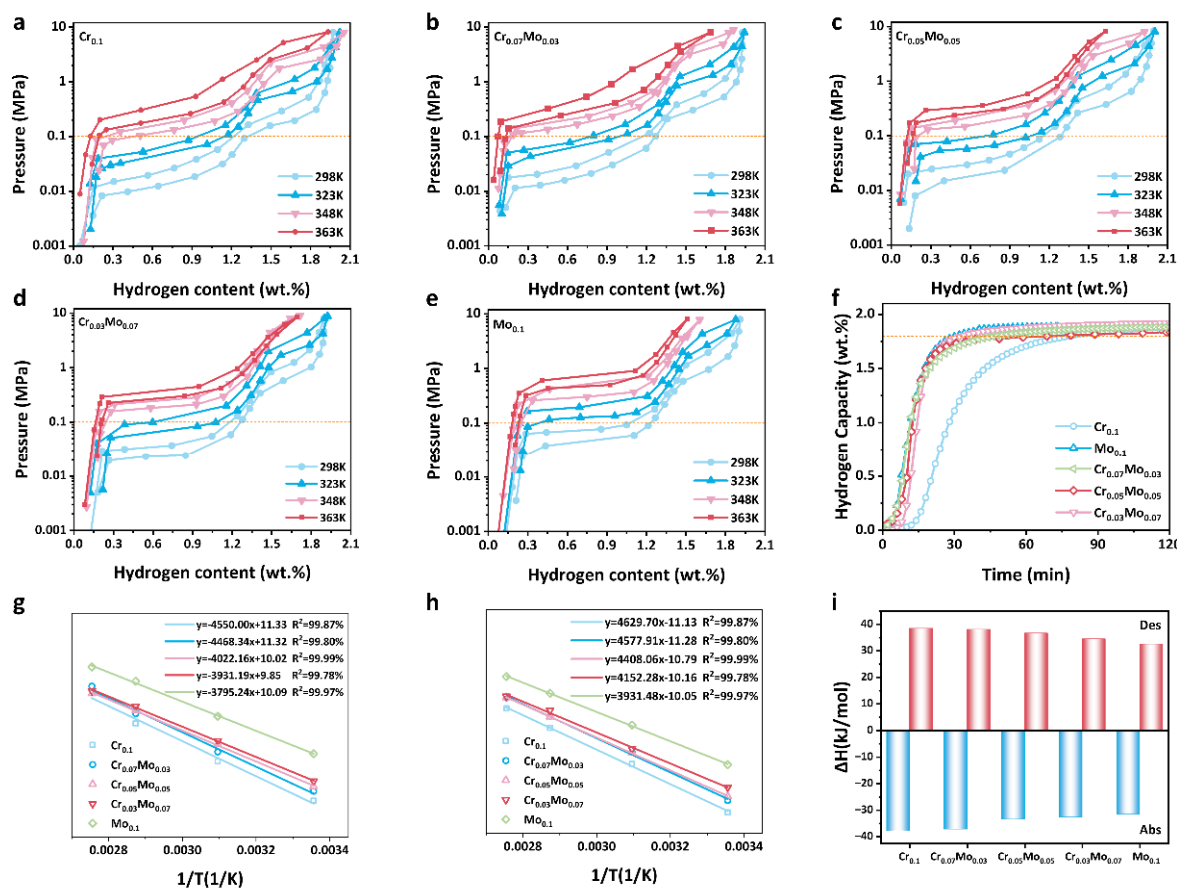


Figure 4. PCT curves of different components at different temperatures: (a) Cr_{0.1}, (b) Cr_{0.07}Mo_{0.03}, (c) Cr_{0.05}Mo_{0.05}, (d) Cr_{0.03}Mo_{0.07}, and (e) Mo_{0.1}. (f) First hydrogen absorption and dehydrogenation kinetics of each component at room temperature. The Van't Hoff equation fits the curve: (g) hydrogen absorption process; (h) hydrogen discharge process; (i) contrast between hydrogen absorption ΔH and desorption ΔH .

Figure 4a–e present the PCT curves and thermodynamic hydrogen absorption/desorption properties of Ti_{1.05}Fe_{0.85}Cr_{0.1-x}Mo_x ($x = 0, 0.03, 0.05, 0.07, 0.1$) alloys at temperatures of 298, 323, 348, and 363 K. The sample Cr_{0.1} exhibits a lower hydrogen ab-/desorption plateau, with the first hydrogen absorption plateau at 0.01–0.02 MPa and 298 K with a relatively sloping plateau, achieving a maximum hydrogen storage capacity of 1.97 wt.%. Mo_{0.1}, on the other hand, has a slightly higher hydrogen ab-/desorption plateau at 0.09 MPa and 298 K with a flatter plateau but a significantly reduced maximum storage capacity of only 1.90 wt.%. As the substitution of Mo for Cr increases, the hydrogen ab-/desorption plateau gradually rises (data for the hydrogen ab-/desorption plateau at 0.6 wt.% are provided in Table S2). At 363 K, Cr_{0.1} achieves a maximum hydrogen storage capacity of 1.93 wt.% and an effective storage capacity of 1.74 wt.%, while Cr_{0.05}Mo_{0.05} reaches a maximum storage capacity of 1.92 wt.% and an effective storage capacity of 1.74 wt.% at 348 K. Cr_{0.1} and Cr_{0.05}Mo_{0.05} exhibit optimal performance at 363 K and 348 K, respectively, reducing the optimal operating temperature (the temperature at which optimal

performance is achieved) by 15 K, making them more suitable for use in hydrogen fuel cells [34,35]. The hydrogen storage capacity of alloys is influenced by factors such as lattice parameters and average relative atomic mass. Due to the small amount of Mo substitution in $\text{Cr}_{0.07}\text{Mo}_{0.03}$, there is a minor change in lattice parameters and a significant variation in average relative atomic mass, leading to a decrease in the maximum storage capacity. As the amount of Mo substitution increases, the change in lattice parameters in $\text{Cr}_{0.05}\text{Mo}_{0.05}$ becomes more significant than the impact of the average relative atomic mass. Further increasing the substitution of Mo results in the lattice parameters having a lesser impact on the maximum storage capacity compared to the average relative atomic mass, ultimately leading to the observed changes in storage capacity. The data for maximum and effective hydrogen storage capacities at various temperatures are listed in Table 3.

By substituting the equilibrium pressures (defined as the pressure corresponding to a hydrogen content of 0.6 wt.%; specific values are listed in Table S2) at different temperatures into the Van't Hoff equation, we can determine ΔH and ΔS through fitting. The specific formula is as follows:

$$\ln(P_{eq}) = \frac{\Delta H}{RT} - \frac{\Delta S}{R} \quad (1)$$

The fitted ΔH and ΔS values show a decreasing trend in the absolute values of ΔH for both hydrogen absorption and desorption. A lower absolute value of ΔH indicates that the hydride is more difficult to form and easier to decompose, which aligns with the changes observed in the hydrogen ab-/desorption plateau. The specific data are provided in Table S3.

3.3. Cycling Performance

Figure 5a exhibits the maximum hydrogen ab-/desorption curves of the $\text{Cr}_{0.05}\text{Mo}_{0.05}$ alloy after undergoing 200 cycles of hydrogen ab-/desorption experiments, demonstrating a stable yet slight decline. Figure 5b,c compare the PCT curves before and after cycling, revealing that the maximum hydrogen storage capacity decreases from 1.99 wt.% to 1.98 wt.%, with a cycling decay of only 0.50%. This alloy exhibits good cycling performance and is a durable hydrogen storage alloy with potential applications. The XRD diffraction patterns of the sample before and after cycling are compared in Figure 5d, where no significant structural changes were observed after 200 cycles. In Figure 5e, the refined curve of the cycled XRD pattern is presented, with the phase abundances of TiFe, $\text{Ti}_{0.8}\text{Fe}_{0.2}$, and β -Ti determined to be 80.36%, 8.84%, and 10.80%, respectively. These values exhibited minimal deviation from those obtained prior to cycling. The variations in lattice parameters are specifically illustrated in Figure 5f. The lattice parameters of the dominant TiFe phase were found to remain nearly constant, whereas slight increases were detected in both the $\text{Ti}_{0.8}\text{Fe}_{0.2}$ and β -Ti phases. The negligible lattice parameter alteration of the main phase was correlated with the preserved PCT curve characteristics after cycling. Such limited structural evolution during extended cycling is proposed to contribute to the enhanced cyclic durability of the material [36,37].

3.4. Comparison with Other TiFe-Based Hydrogen Storage Alloys

Table 4 lists the maximum hydrogen storage capacity, effective hydrogen storage capacity, number of activation cycles, activation temperature, and activation hydrogen pressure for several TiFe-based hydrogen storage alloys. Both compositions, $\text{Cr}_{0.1}$ and $\text{Cr}_{0.05}\text{Mo}_{0.05}$, from this work demonstrated favorable performance across all these indicators. They hold potential guidance significance for enhancing the activation performance and hydrogen absorption/desorption properties of TiFe-based hydrogen storage alloys.

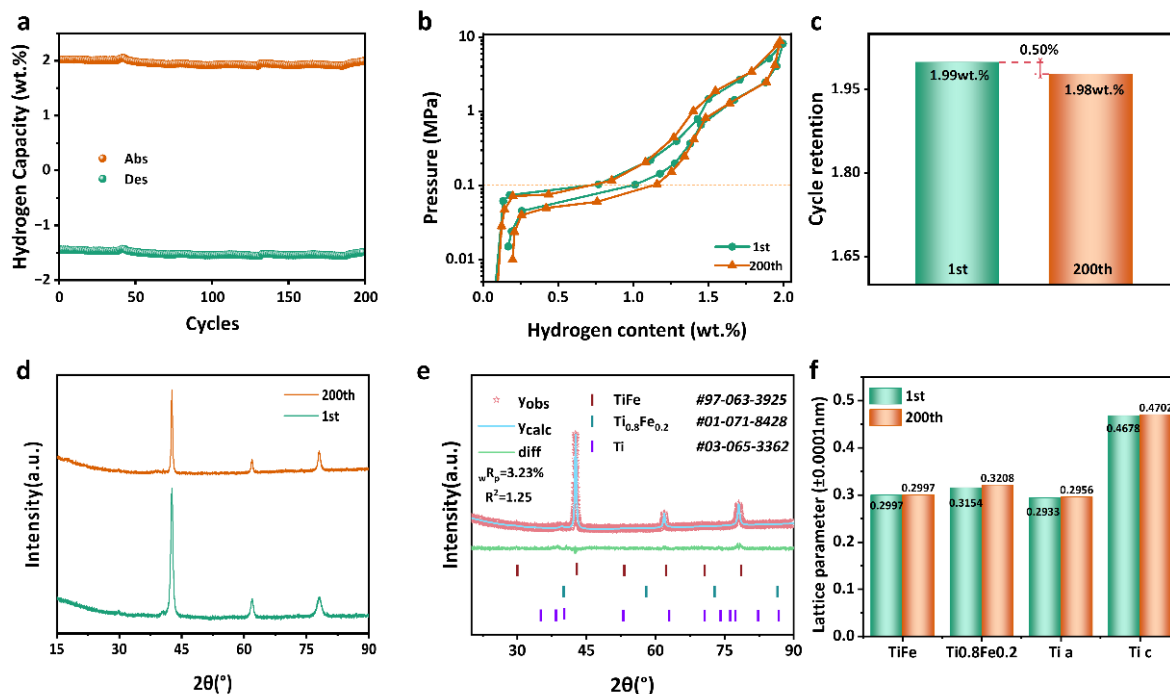


Figure 5. (a) The relationship between the number of cycles of the Cr_{0.05}Mn_{0.05} sample and the amount of hydrogen absorption and discharge; (b) 1st and 200th PCT curves; (c) capacity attenuation diagram; (d) comparison of XRD diffraction patterns before and after cycling; (e) refined XRD pattern after cycling; (f) comparison of lattice parameter changes after refinement.

Table 4. Comparison of maximum hydrogen storage capacity (C_M), effective hydrogen storage capacity (C_E), number of activation cycles (N_A), activation temperature (T_A), and activation hydrogen pressure (P_A) for TiFe-based hydrogen storage alloys.

Component	C_M (wt.%)	C_E (wt.%)	N_A	T_A (K)	P_A (MPa)	Ref.
Ti _{1.1} Fe _{0.8} Mn _{0.2}	1.88	1.58	2	423	4	[38]
TiFe _{0.8} Al _{0.2}	1.2	0.4	1	323	4	[39]
Ti _{1.04} Pr _{0.06} Fe _{0.8} Mn _{0.2}	1.75	1.55	1	373	4	[40]
TiFe	1.86	1.7	>3	673	6.5	[15]
Ti _{1.08} Y _{0.02} Fe _{0.8} Mn _{0.2}	1.85	1.55	3	373	4	[41]
TiFe _{0.9} Cr _{0.1}	1.7	1.3	1	303	4	[22]
Ti _{0.99} La _{0.01} Fe _{0.8} Mn _{0.2}	1.78	1.48	1	423	3	[29]
THIS WORK	1.92	1.74	1	298	4	

4. Conclusions

In summary, the Ti_{1.05}Fe_{0.85}Cr_{0.1-x}Mo_x ($x = 0, 0.03, 0.05, 0.07, 0.1$) alloys exhibited three phases—TiFe, Ti_{0.8}Fe_{0.2}, and β -Ti—due to the introduction of Cr and Mo, as well as excess Ti. The lattice constant of the primary TiFe phase increased upon substitution with Cr and Mo, which have larger atomic radii than that of Fe. Conversely, the lattice constants of Ti_{0.8}Fe_{0.2} and β -Ti decreased due to the substitution of Ti with Cr, Mo, and Fe, which have smaller atomic radii. As Mo was substituted for Cr, the activation performance of the alloys gradually improved, and the hydrogen absorption/desorption plateaus increased, resulting in room-temperature activation and suitable hydrogen absorption/desorption plateaus for the Cr_{0.05}Mn_{0.05} composition. This alloy achieved a maximum hydrogen storage capacity of 1.93 wt.% and an effective hydrogen storage capacity of 1.73 wt.% at 348 K. After 200 hydrogen absorption/desorption cycles at room temperature, the capacity

decay of the Cr_{0.05}Mo_{0.05} alloy was only 0.50%. Therefore, this alloy has potential as a solid-state hydrogen storage material suitable for hydrogen fuel cells.

Supplementary Materials: The following supporting information can be downloaded at <https://www.mdpi.com/article/10.3390/met15020200/s1>. Figure S1. The refined XRD diffraction patterns of Cr_{0.07}Mo_{0.03} (a) and Cr_{0.03}Mo_{0.07} (b); Table S1. Comparison of lattice parameters, phase abundance, R_{wp} and R² of different samples after refinement; Figure S2. The HRTEM images of the Cr_{0.1} and Mo_{0.1} alloys; Table S2. Equilibrium pressure of the ab-/desorption are from Hydrogen content 0.6 wt.%; Table S3. The ΔH_{abs}, ΔH_{des}, ΔS_{abs} and ΔS_{des} of different composition.

Author Contributions: Methodology, M.Z.; software, M.Z.; formal analysis, Y.L. and H.X.; investigation, H.X.; resources, M.Z.; data curation, Y.L. and H.X.; writing—original draft, Y.L.; writing—review and editing, Y.L., H.X. and Q.C.; supervision, M.Z. and Q.C.; project administration, Q.C.; funding acquisition, Q.C. All authors have read and agreed to the published version of the manuscript.

Funding: This research was funded by the National Key R&D Program of China (2022YFB3504700).

Data Availability Statement: The original contributions presented in this study are included in the article/supplementary material. Further inquiries can be directed to the corresponding authors.

Conflicts of Interest: The authors declare no conflict of interest.

References

- Ang, T.-Z.; Salem, M.; Kamarol, M.; Das, H.S.; Nazari, M.A.; Prabaharan, N. A comprehensive study of renewable energy sources: Classifications, challenges and suggestions. *Energy Strategy Rev.* **2022**, *43*, 100939. [[CrossRef](#)]
- Şen, Z. Solar energy in progress and future research trends. *Prog. Energy Combust. Sci.* **2004**, *30*, 367–416. [[CrossRef](#)]
- Shim, J.-H.; Kim, S.-W.; Baik, J.M. Advanced materials for carbon neutrality: Energy conversion, Hydrogen storage, and CO₂ capture and conversion. *Nano Energy* **2023**, *115*, 108726. [[CrossRef](#)]
- Msigwa, G.; Ighalo, J.O.; Yap, P.S. Considerations on environmental, economic, and energy impacts of wind energy generation: Projections towards sustainability initiatives. *Sci. Total Environ.* **2022**, *849*, 157755. [[CrossRef](#)]
- Martínez, M.L.; Vázquez, G.; Pérez-Maqueo, O.; Silva, R.; Moreno-Casasola, P.; Mendoza-González, G.; López-Portillo, J.; MacGregor-Fors, I.; Heckel, G.; Hernández-Santana, J.R.; et al. A systemic view of potential environmental impacts of ocean energy production. *Renew. Sustain. Energy Rev.* **2021**, *149*, 111332. [[CrossRef](#)]
- Chu, S.; Majumdar, A. Opportunities and challenges for a sustainable energy future. *Nature* **2012**, *488*, 294–303. [[CrossRef](#)]
- Alola, A.A.; Olanipekun, I.O.; Shah, M.I. Examining the drivers of alternative energy in leading energy sustainable economies: The trilemma of energy efficiency, energy intensity and renewables expenses. *Renew. Energy* **2023**, *202*, 1190–1197. [[CrossRef](#)]
- Farghali, M.; Osman, A.I.; Mohamed, I.M.A.; Chen, Z.; Chen, L.; Ihara, I.; Yap, P.S.; Rooney, D.W. Strategies to save energy in the context of the energy crisis: A review. *Environ. Chem. Lett.* **2023**, *21*, 2003–2039. [[CrossRef](#)] [[PubMed](#)]
- Rasul, M.G.; Hazrat, M.A.; Sattar, M.A.; Jahirul, M.I.; Shearer, M.J. The future of hydrogen: Challenges on production, storage and applications. *Energy Convers. Manag.* **2022**, *272*, 116326. [[CrossRef](#)]
- Yue, M.; Lambert, H.; Pahon, E.; Roche, R.; Jemei, S.; Hissel, D. Hydrogen energy systems: A critical review of technologies, applications, trends and challenges. *Renew. Sustain. Energy Rev.* **2021**, *146*, 111180. [[CrossRef](#)]
- Abdechafik, E.H.; Ousaleh, H.A.; Mehmood, S.; Baba, Y.F.; Bürger, I.; Linder, M.; Faik, A. An analytical review of recent advancements on solid-state hydrogen storage. *Int. J. Hydrogen Energy* **2024**, *52*, 1182–1193. [[CrossRef](#)]
- Li, C.; Yang, W.; Liu, H.; Liu, X.; Xing, X.; Gao, Z.; Dong, S.; Li, H. Picturing the Gap Between the Performance and US-DOE’s Hydrogen Storage Target: A Data-Driven Model for MgH₂ Dehydrogenation. *Angew. Chem. Int. Ed.* **2024**, *63*, e202320151. [[CrossRef](#)] [[PubMed](#)]
- Li, Z.-Y.; Sun, Y.-J.; Zhang, C.-C.; Wei, S.; Zhao, L.; Zeng, J.-L.; Cao, Z.; Zou, Y.-J.; Chu, H.-L.; Xu, F.; et al. Optimizing hydrogen ad-/desorption of Mg-based hydrides for energy-storage applications. *J. Mater. Sci. Technol.* **2023**, *141*, 221–235. [[CrossRef](#)]
- Sun, X.; Yang, X.; Lu, Y.; Luo, Q.; Wu, C.; Zhang, Y.; Lyu, T.; Gu, Q.; Li, Q.; Pan, F. Hot extrusion-induced Mg-Ni-Y alloy with enhanced hydrogen storage kinetics. *J. Mater. Sci. Technol.* **2024**, *202*, 119–128. [[CrossRef](#)]
- Reilly, J.J.; Wiswall, J.R.H. Formation and Properties of Iron Titanium Hydride. *Inorg. Chem.* **1974**, *13*, 218–222. [[CrossRef](#)]
- Yartys, V.A.; Lototskyy, M.V. Laves type intermetallic compounds as hydrogen storage materials: A review. *J. Alloys Compd.* **2022**, *916*, 165219. [[CrossRef](#)]
- Padhee, S.P.; Roy, A.; Pati, S. Role of Mn-substitution towards the enhanced hydrogen storage performance in FeTi. *Int. J. Hydrogen Energy* **2022**, *47*, 9357–9371. [[CrossRef](#)]

18. Reilly, J.J.; Johnson, J.R. *Metal Hydride Materials Program at BNL: Current Status and Future Plans*; U.S. Department of Energy Office of Scientific and Technical Information: Oak Ridge, TN, USA, 1976.
19. Sandrock, G.D.; Goodell, P.D. Surface Poisoning of LaNi₅, FeTi and (Fe,Mn)Ti by O₂, Co and H₂O. *J. Less-Common Met.* **1980**, *73*, 161–168. [[CrossRef](#)]
20. Dematteis, E.M.; Berti, N.; Cuevas, F.; Latroche, M.; Baricco, M. Substitutional effects in TiFe for hydrogen storage: A comprehensive review. *Mater. Adv.* **2021**, *2*, 2524–2560. [[CrossRef](#)]
21. Jung, J.Y.; Lee, S.-I.; Faisal, M.; Kim, H.; Lee, Y.-S.; Suh, J.-Y.; Shim, J.-H.; Huh, J.-Y.; Cho, Y.W. Effect of Cr addition on room temperature hydrogenation of TiFe alloys. *Int. J. Hydrogen Energy* **2021**, *46*, 19478–19485. [[CrossRef](#)]
22. Kwon, H.G.; Park, K.B.; Fadonougbo, J.O.; Kim, N.-S.; Kwak, R.-H.; Lee, D.H.; Park, C.-S.; Kim, Y.D.; Ko, W.-S.; Park, H.-K. Study on the microstructure and hydrogen storage property changes of cast TiFe_{0.9}Cr_{0.1} alloy by homogenization annealing. *Mater. Chem. Phys.* **2023**, *309*, 128362. [[CrossRef](#)]
23. Park, K.B.; Ko, W.-S.; Fadonougbo, J.O.; Na, T.-W.; Im, H.-T.; Park, J.-Y.; Kang, J.-W.; Kang, H.-S.; Park, C.-S.; Park, H.-K. Effect of Fe substitution by Mn and Cr on first hydrogenation kinetics of air-exposed TiFe-based hydrogen storage alloy. *Mater. Charact.* **2021**, *178*, 111246. [[CrossRef](#)]
24. Haiqin, D.J.Q.; Chaohui, P.; Yongqiang, N.; Tiesheng, H.; Zhilin, L.; Yuwan, L.; Zhu, W. Effects of Cs₀ introduction on hydrogen storage properties of Ti–Fe–Mn alloys. *Int. J. Hydrogen Energy* **2015**, *40*, 2729–2735. [[CrossRef](#)]
25. Lee, S.-M.; Perng, T.-P. Effect of the second phase on the initiation of hydrogenation of TiFe_{1-x}M_x (M = Cr,Mn) alloys. *Int. J. Hydrogen Energy* **1993**, *19*, 259–263. [[CrossRef](#)]
26. Ha, T.; Kim, J.-H.; Sun, C.; Lee, Y.-S.; Kim, D.-I.; Suh, J.-Y.; Jang, J.-I.; Lee, J.; Kim, Y.; Shim, J.-H. Crucial role of Ce particles during initial hydrogen absorption of AB-type hydrogen storage alloys. *Nano Energy* **2023**, *112*, 108483. [[CrossRef](#)]
27. Shang, Y.L.H.; Zhang, Y.; Qi, Y.; Guo, S.; Zhao, D. Structure and hydrogenation performances of as-cast Ti_{1.1-x}RE_x Fe_{0.8}Mn_{0.2} (RE = Pr, Sm and Nd; x = 0, 0.01) alloys. *Int. J. Hydrogen Energy* **2018**, *43*, 19091–19101. [[CrossRef](#)]
28. Yuan, Z.-M.; Qi, Z.; Zhai, T.-T.; Wang, H.-Z.; Wang, H.-Y.; Zhang, Y.-H. Effects of La substitution on microstructure and hydrogen storage properties of Ti–Fe–Mn-based alloy prepared through melt spinning. *Trans. Nonferrous Met. Soc. China* **2021**, *31*, 3087–3095. [[CrossRef](#)]
29. Zhai, T.; Wei, Z.; Yuan, Z.; Han, Z.; Feng, D.; Wang, H.; Zhang, Y. Influences of La addition on the hydrogen storage performances of TiFe-base alloy. *J. Phys. Chem. Solids* **2021**, *157*, 110176. [[CrossRef](#)]
30. Alam, M.M.; Sharma, P.; Huot, J. Effect of addition of rare earth element La on the hydrogen storage properties of TiFe alloy synthesized by mechanical alloying. *Int. J. Hydrogen Energy* **2023**, *50*, 261–271. [[CrossRef](#)]
31. Dematteis, E.M.; Barale, J.; Capurso, G.; Deledda, S.; Sørby, M.H.; Cuevas, F.; Latroche, M.; Baricco, M. In-situ neutron diffraction during reversible deuterium loading in Ti-rich and Mn-substituted Ti(Fe,Mn)_{0.90} alloys. *J. Alloys Compd.* **2023**, *935*, 168150. [[CrossRef](#)]
32. Ma, H.P.J.; Wang, X.; Chen, C.; Wang, Q. Hydrogen storage properties of FeTi_{1.3+x} wt%Mm (x = 0.0, 1.5, 3.0, 4.5, 6.0) hydrogen storage alloys. *Int. J. Hydrogen Energy* **2000**, *25*, 779–782. [[CrossRef](#)]
33. Park, K.B.; Na, T.-W.; Kim, Y.D.; Park, J.-Y.; Kang, J.-W.; Kang, H.-S.; Park, K.; Park, H.-K. Characterization of microstructure and surface oxide of Ti_{1.2}Fe hydrogen storage alloy. *Int. J. Hydrogen Energy* **2021**, *46*, 13082–13087. [[CrossRef](#)]
34. Guo, X.; Li, W.; Ren, D.; Chu, J. Prospects for the development of hydrogen fuel cell vehicles in China. *Renew. Energy* **2025**, *240*, 122231. [[CrossRef](#)]
35. Olabi, A.G.; Sayed, E.T. Developments in Hydrogen Fuel Cells. *Energies* **2023**, *16*, 2431. [[CrossRef](#)]
36. Itoh, H.; Arashima, H.; Kubo, K.; Kabutomori, T.; Ohnishi, K. Improvement of cyclic durability of BCC structured Ti–Cr–V alloys. *J. Alloys Compd.* **2005**, *404–406*, 417–420. [[CrossRef](#)]
37. Wu, Y.; Zhao, W.; Jiang, L.; Li, Z.; Guo, X.; Ye, J.; Yuan, B.; Wang, S.; Hao, L. Effect of Fe and Al on hydrogen storage properties of 75 V-Ti-Cr alloys. *J. Alloys Compd.* **2021**, *887*, 161181. [[CrossRef](#)]
38. Shang, H.; Zhang, Y.; Li, Y.; Qi, Y.; Guo, S.; Zhao, D. Effects of adding over-stoichiometrical Ti and substituting Fe with Mn partly on structure and hydrogen storage performances of TiFe alloy. *Renew. Energy* **2019**, *135*, 1481–1498. [[CrossRef](#)]
39. Kwon, H.G.; Jung, S.; Ko, W.-S.; Kwak, R.-H.; Lee, D.H.; Na, T.-W.; Kim, S.; Park, S.; Park, H.-K. Microstructural study on the slope of plateau pressure in TiFe0.8Al0.2 hydrogen storage alloy. *Mater. Lett.* **2024**, *360*, 135951. [[CrossRef](#)]
40. Li, C.; Liu, B.; Li, Y.; Yuan, Z.; Zhou, D.; Wang, H. A significantly improved hydrogen storage performance of nanocrystalline Ti–Fe–Mn–Pr alloy. *J. Mater. Res. Technol.* **2023**, *23*, 4566–4575. [[CrossRef](#)]
41. Li, C.; Lan, Y.; Wei, X.; Zhang, W.; Liu, B.; Gao, X.; Yuan, Z. Improvement of hydrogen absorption and desorption properties of TiFe-based alloys by adding yttrium. *J. Alloys Compd.* **2022**, *927*, 166992. [[CrossRef](#)]

Disclaimer/Publisher’s Note: The statements, opinions and data contained in all publications are solely those of the individual author(s) and contributor(s) and not of MDPI and/or the editor(s). MDPI and/or the editor(s) disclaim responsibility for any injury to people or property resulting from any ideas, methods, instructions or products referred to in the content.